International Journal of Heat and Mass Transfer 52 (2009) 4327–4342

Contents lists available at ScienceDirect

International Journal of Heat and Mass Transfer

journal homepage: www.elsevier.com/locate/ijhmt

Vascularization with line-to-line trees in counterflow heat exchange

Houlei Zhang [a,*], Sylvie Lorente [b], Adrian Bejan [c]

[a] School of Power Engineering, Nanjing University of Science and Technology, Nanjing 210094, China
[b] Université de Toulouse, UPS, INSA, LMDC (Laboratoire Matériaux et Durabilité des Constructions), 135, Avenue de Rangueil, F-31 077 Toulouse Cedex 04, France
[c] Department of Mechanical Engineering and Materials Science, Duke University, Durham, NC 27708-0300, USA

ARTICLE INFO

Article history:
Received 12 September 2008
Received in revised form 17 March 2009
Accepted 31 March 2009
Available online 18 May 2009

Keywords:
Constructal
Vascularization
Dendritic
Line-to-line trees
Heat exchangers
Svelteness

ABSTRACT

Here we report the heat and fluid flow characteristics of counterflow heat exchangers with tree-shaped line-to-line flow channels. The flow structures of the hot and cold sides are sequences of point-to-line trees that alternate with upside-down trees. The paper shows under what conditions the tree vascularization offers greater heat flow access than corresponding conventional designs with parallel single-scale channels. The analytical part is based on assuming fully developed laminar flow in every channel and negligible longitudinal conduction in the solid. The numerical part consists of simulations of three-dimensional convection coupled with conduction in the solid. It is shown that tree vascularization offers greater heat flow access (smaller global thermal resistance) than parallel channels when the number of pairing levels increases and the available pumping power or pressure drop is specified. When the solid thermal conductivity increases, the heat transfer effectiveness decreases because of the effect of longitudinal heat conduction. The nonuniformity in fluid outlet temperature becomes more pronounced when the number of pairing levels increases and the pumping power (or pressure drop number) increases. The nonuniformity in outlet fluid temperature decreases when the solid thermal conductivity increases.

1. Introduction

Vascularized (tree shaped) convective configurations dominate the design of natural flow structures. They are finding more and more applications in advanced engineering areas, such as distributed cooling and heating, self-healing, etc. [1–4]. In Ref. [5], tree-shaped conducting paths for cooling a heat generating volume were first deduced based on a general principle (i.e. constructal law). Based on constructal law, Bejan and Errera [6] outlined a method for constructing the architecture of the volume-to-point path with minimal flow resistance. The feature of the minimal-resistance flow path is that the high-permeability channels of the various volume elements form a tree network which is deterministic. Inspired by natural flow systems, Chen and Cheng [7] studied a new design of fractal branch channel networks with different dimensions and different branching levels for cooling electronic chips. Compared with the traditional parallel channels, the new flow structure offers greater heat transfer capability and consumes less pumping power. In their later experimental work, Chen and Cheng [8,9] fabricated MEMS technology-based tree-shaped microchannel heat sinks and tested the cooling performance. The experimental results confirm that the thermal efficiency of the tree-shaped microchannel heat sinks is much higher than that of the traditional parallel channels.

According to constructal theory [10–12], the flow structures that maximize the global performance of a macroscopic flow system accessed volumetrically by streams from concentrated ports are tree-shaped (multiscale, nonuniform), not parallel and uniform. By relying on the contructal method, Ref. [13] proposed the conceptual design of a constructal two-stream heat exchanger with small-scale crossflows and large-scale counterflows. Such heat exchangers have been built, tested, and analyzed based on three-dimensional simulations [13,14]: the main conclusion is that the proposed tree-like heat exchanger structure offers definite advantages over the use of parallel channels in fully developed laminar region.

More recently, da Silva et al. [15] described the conceptual design and performance of constructal dendritic two-stream counterflow heat exchangers, where both sides of the heat transfer surface are bathed by tree-shaped flow on a disc. They reported the relationships between effectiveness and number of heat transfer units for several tree-shaped counterflow configurations, and showed the superior performance of the constructal design. This design concept was tested in experiments with two compact disc-like tree-shaped structures [16].

In the search for flow configurations with two objectives (low fluid-flow resistance and low thermal resistance), Ref. [17]

* Corresponding author. Tel.: +86 25 84316541; fax: +86 25 84312432.
E-mail address: houlei_zhang@yahoo.com.cn (H. Zhang).

0017-9310/$ - see front matter © 2009 Elsevier Ltd. All rights reserved.
doi:10.1016/j.ijheatmasstransfer.2009.03.064

Nomenclature

A	covered area (in x–y plane)
A_{ij}	local heat transfer area, Eq. (11)
Be	Bejan number, Eq. (20)
c_p	specific heat at constant pressure
C_s	ratio of successive channel widths, Eq. (2)
d	elemental length, Figs. 1 and 2
D_h	hydraulic diameter
h	depth of fluid channels, Figs. 1 and 2
$\tilde{h}$	dimensionless depth of fluid channels, $\tilde{h} = h/Z$
h_i	local heat transfer coefficient in one fluid channel
i	order of pairing levels
k	fluid thermal conductivity
k_s	solid thermal conductivity
$\tilde{k}_s$	dimensionless solid thermal conductivity, $\tilde{k}_s = k_s/k_{steel}$
k_{steel}	thermal conductivity of steel
L	channel length
M	dimensionless flow rate
$\dot{m}$	mass flow rate
$\dot{m}_a$	mass flow rate, tree a, Fig. 1
$\dot{m}_{aij}$	mass flow rate in the jth channel of rank i of tree a, Fig. 2
$\dot{m}_b$	mass flow rate, tree b, Fig. 1
n	number of pairing levels
N	number of heat transfer units
Nu	Nusselt number
P	pressure
P_i	inlet pressure
P_o	outlet pressure
q	heat transfer rate
$\tilde{R}$	dimensionless thermal resistance based on total volume
Re	Reynolds number (for trees, Re refers to the trunk channel)
S	width of rectangular cross-section of flow channels
Sv	svelteness number
t	wall thickness between two channels, Fig. 1
T	temperature
$\tilde{T}_{ho}$	dimensionless outlet hot fluid temperature
u, v, w	velocity components in x, y, z directions
U	overall heat transfer coefficient
V	total volume
V_f	total flow volume
$\dot{W}'''$	per-unit-volume pumping power
$\dot{W}$	pumping power
$\tilde{W}$	dimensionless pumping power
x, y, z	coordinates
X, Y, Z	dimensions of vascularized unit, Fig. 1

Greek symbols

α	thermal diffusivity of fluid
ΔP	pressure drop
ΔT_f	temperature variation along the stream
ΔT_i	inlet temperature difference between two streams
ΔT_m	temperature difference
ΔV_f	volume modification due to special geometry at junctions, inlets and outlets, Eq. (4)
Ω	heat transfer nonuniformity based on trees a and b, Eq. (26a)
Ω_a	heat transfer nonuniformity based on tree a, Eq. (26b)
ε	effectiveness of heat transfer
μ	dynamic viscosity
ρ	fluid density
ν	kinematic viscosity
ϕ	porosity, Eq. (3)

Superscripts

i	pairing level, or rank
n	number of pairing levels

Subscripts

0	the trunk of a tree
a, b	trees a and b, Fig. 2
ave	average
c	cold stream
cold	cold stream
f	fluid
h	hot stream
hot	hot stream
i	pairing level, or inlet
in	inlet
j	channels of the same rank, Fig. 2
max	maximum
min	minimum
n	number of pairing levels
o	outlet
out	outlet
s	solid

proposed the concept of line-to-line tree-shaped flow architectures, Fig. 1, as a substitute for the use of parallel channels which have been typical architectures in cooling electronics (Fig. 2). For channels with round cross-section, Ref. [17] showed analytically that when the number of pairing levels is 4 or larger, the tree-shaped flow structures offer greater access to the flow than parallel channels. For channels with rectangular cross-section with the same constructal structure as in Ref. [17], it was shown analytically and numerically [18] that tree vascularization is more attractive in offering greater flow access than parallel channels when the number of bifurcation levels increases, the global porosity of the vascularized body decreases, and the global svelteness of the flow architecture increases. In the present paper, we develop numerically the heat transfer characteristics of vascular systems with line-to-line tree counterflow fluid channels (Fig. 1), and compare their performance with that of traditional designs (Fig. 2). We also study the validity of using conventional analytical methods for counterflow heat exchangers in vascularized heat exchangers.

2. Heat transfer analysis

2.1. Geometry

As an example, the tree-shaped architecture with two pairing levels is shown in Fig. 1. In the top and middle drawings, the lines indicate the positions of the flow channels, without showing the cross-sectional dimensions. Four constraints are specified for the flow configurations of Figs. 1 and 2: the total unit volume V, the total flow volume V_f, the elemental length d, and the fluid cross-sectional depth h.

Fig. 3 defines how dendritic and parallel-channels designs will be compared. The dimensions (X, Y, Z) of the two types of structures are the same: note the same X in the horizontal direction, Fig. 3. When different tree structures are compared in the vertical direction in Fig. 3 (e.g., $n = 2$ and 3), the elemental length d is fixed but X and Y vary. The dimension Y ($n = 3$) is the flow length of the structure (trees, or parallel channels) that correspond to three levels of pairing or bifurcation.

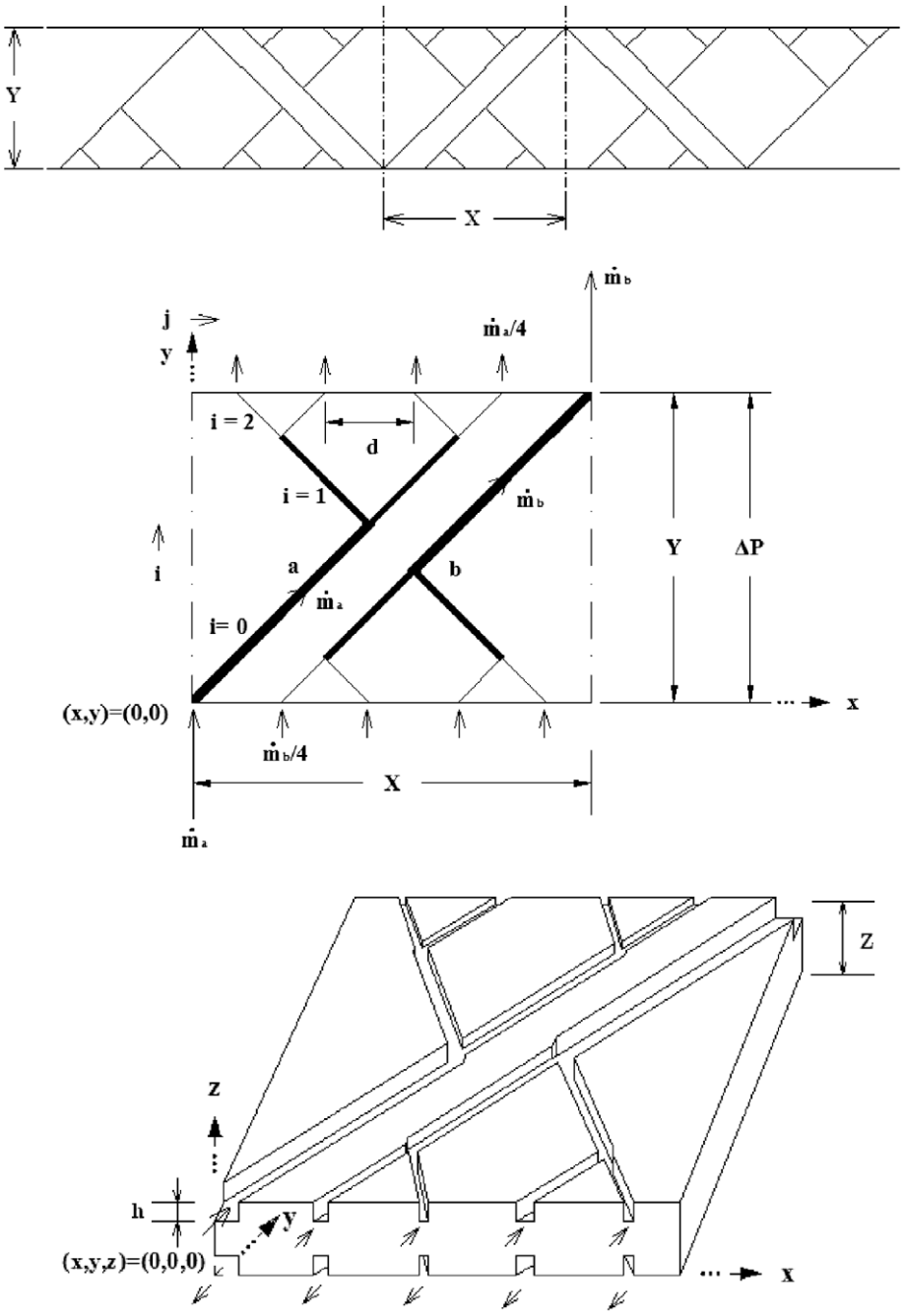

Fig. 1. Layout of tree-shaped channels that are machined into the upper and lower *XY* surfaces of the volume element shown in this figure. The middle drawing shows the flow direction over the upper side of the slab. On the lower side the tree architecture is exactly the same, but the flow is in the opposite direction. Note that the flow rate through the trunk (port 5) is approximately four times the flow rate through the smallest channels of the canopy (ports 1–4).

The optimization of the geometry of the tree-shaped architecture is documented in Ref. [17], and is not repeated here. The geometrical features in Fig. 1 are expressed by the relations

$$X = (2^n + 1/2)d \quad Y = (2^n - 1/2)d \quad Z = 2h + t \tag{1}$$

$$L_n/d = 2^{-1/2} \quad L_{i-1}/L_i = 2 \quad C_S = S_{i-1}/S_i = 2^{2/3} \tag{2}$$

$$\phi = \frac{V_f}{V} \quad \mathrm{Sv} = \frac{Y}{V_f^{1/3}} \tag{3}$$

The total flow volume is

$$V_f = 4\sum_{i=0}^{n}(2^i L_i S_i h) - \Delta V_f \tag{4}$$

where the volume correction ΔV_f depends on the special geometries at junctions, inlets and outlets (Fig. 4). The svelteness number Sv is defined as the ratio of the external length scale divided by the internal length scale [19]. The two counterflow streams flow through identical configurations of flow channels. They differ only with respect to inlet temperatures and flow directions.

2.2. Effectiveness

The local heat transfer rate at one hot–cold fluid channel pair (Fig. 1), i.e. channel (i, j) is

$$q_{aij} = U_i A_{ij} \Delta T_{mi} \tag{5a}$$

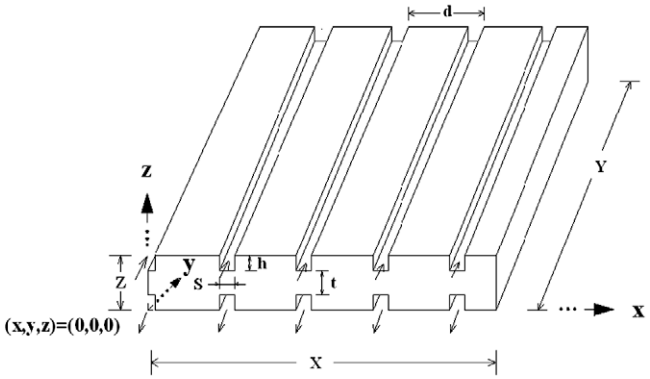

Fig. 2. Volume element (*XYZ*) vascularized with two sets of parallel channels in counterflow.

The total heat transfer rate of one hot-to-cold tree-to-tree structure is

$$q_a = \sum_{i=0}^{n} 2^i q_{aij} \tag{5b}$$

We assume that the effect of heat conduction through the solid material is negligible. The overall heat transfer coefficient is

$$\frac{1}{U_i} = \frac{1}{h_i} + \frac{1}{h_i} = \frac{2}{h_i} \tag{6}$$

where h_i is the heat transfer coefficient for hydrodynamically and thermally fully developed laminar flow in one channel

$$h_i = \frac{k}{D_{hi}} \mathrm{Nu}_i \tag{7}$$

The local heat transfer rate q_{aij} is also equal to the enthalpy change experienced longitudinally by one stream

$$q_{aij} = \dot{m}_{aij} c_p \Delta T_{fi} \tag{8a}$$

The total heat transfer rate is calculated by summing up the longitudinal enthalpy changes

$$q_a = \sum_{i=0}^{n} 2^i \dot{m}_{aij} c_p \Delta T_{fi} \tag{8b}$$

By dividing Eqs. (5a) and (8a) we find the number of heat transfer units

$$N_i = \frac{\Delta T_{fi}}{\Delta T_{mi}} = \frac{k \mathrm{Nu}_i A_{ij}}{2 \dot{m}_{aij} c_p D_{hi}} \tag{9}$$

It was shown in Ref. [15] that ΔT_{mi} does not depend on the rank and position (i) of two channels (of the same size) in counterflow, i.e. $\Delta T_{mi} = \Delta T_m$, so that the global number of heat transfer units assumes the form

$$N = \frac{\Delta T_f}{\Delta T_m} = \frac{k}{2 \dot{m}_a c_p} \sum_{i=0}^{n} \frac{2^i \mathrm{Nu}_i A_{ij}}{D_{hi}} \tag{10}$$

where

$$A_{ij} = (S_i + 2h) L_i \tag{11}$$

$$D_{hi} = \frac{2 S_i h}{S_i + h} \tag{12}$$

and Nu_i is calculated by using the data for rectangular ducts reported in Shah and London [20]. The effectiveness (ε) relation for a counterflow of trees is the same as the conventional relation for two streams in counterflow [15]

$$\varepsilon = \frac{N}{1 + N} \tag{13}$$

The analysis presented above is valid for the conventional counterflow configuration: heat exchangers in which the fluid volume fraction (porosity) is high and longitudinal heat conduction in solid is negligible. In the present paper ϕ is not large, and this means that the domain of applicability of the conventional analytical method needs to be verified. To this question we return in Section 4.

3. Numerical modeling

The heat and fluid flow performance of the counterflow is simulated numerically by using a model for three-dimensional conjugated heat transfer. The basic assumptions are: (1) steady laminar flow, (2) no heat generation in the solid, (3) constant properties for

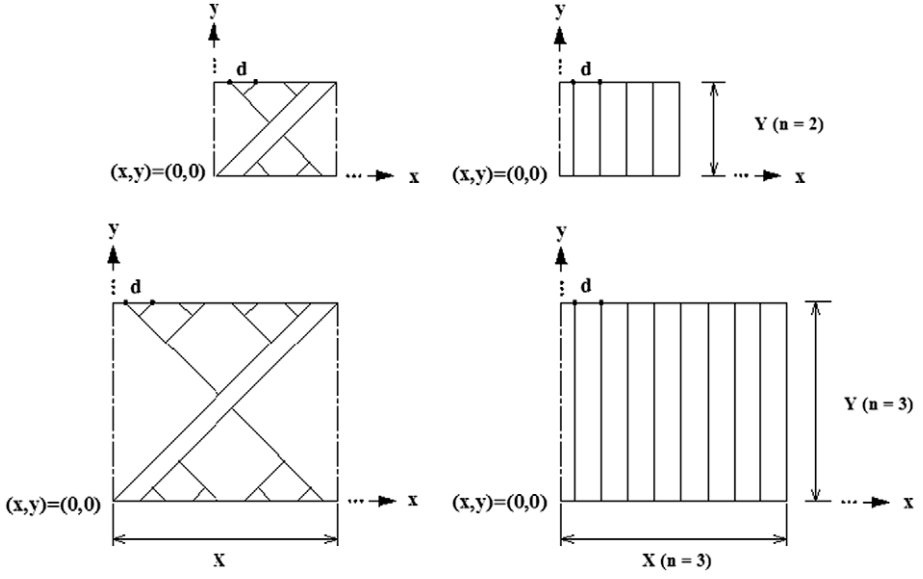

Fig. 3. Tree structures (n = 2, 3) and corresponding parallel channels with $Y = Y$.

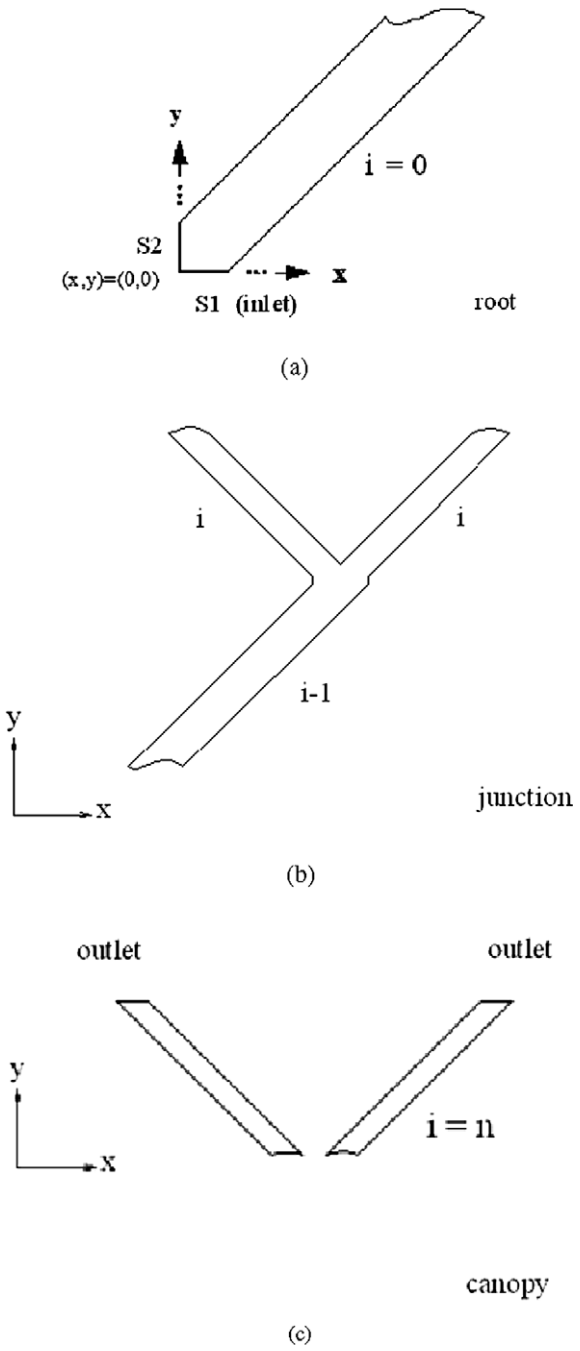

Fig. 4. The geometry of inlets, junctions and outlets projected on the plane x–y.

both fluid and solid, (4) incompressible fluid, e.g., water. The governing equations for fluid flow are

$$\frac{\partial u}{\partial x}+\frac{\partial v}{\partial y}+\frac{\partial w}{\partial z}=0 \tag{14}$$

$$u\frac{\partial u}{\partial x}+v\frac{\partial u}{\partial y}+w\frac{\partial u}{\partial z}=-\frac{1}{\rho}\frac{\partial P}{\partial x}+\nu\nabla^2 u \tag{15}$$

$$u\frac{\partial v}{\partial x}+v\frac{\partial v}{\partial y}+w\frac{\partial v}{\partial z}=-\frac{1}{\rho}\frac{\partial P}{\partial y}+\nu\nabla^2 v \tag{16}$$

$$u\frac{\partial w}{\partial x}+v\frac{\partial w}{\partial y}+w\frac{\partial w}{\partial z}=-\frac{1}{\rho}\frac{\partial P}{\partial z}+\nu\nabla^2 w \tag{17}$$

$$u\frac{\partial T_f}{\partial x}+v\frac{\partial T_f}{\partial y}+w\frac{\partial T_f}{\partial z}=\alpha\nabla^2 T_f \tag{18}$$

where $\nabla^2=\partial^2/\partial x^2+\partial^2/\partial y^2+\partial^2/\partial z^2$. The equation for heat conduction in the solid is

$$\nabla^2 T_s=0 \tag{19}$$

The frame (x, y, z) is aligned with the (X, Y, Z) directions shown in Figs. 1 and 2. The boundary conditions are

Hot stream (the upper stream, Figs. 1 and 2)

$y = 0$: $P = P_i$, $T_f = T_{hi}$
$y = Y$: $P = P_o$
S2: plane of symmetry (Fig. 4)
$z = Z$: non-slip wall

Cold stream (the lower stream, Figs. 1 and 2)

$y = 0$: $P = P_o$
$y = Y$: $P = P_i$, $T_f = T_{ci}$
S2: plane of symmetry (Fig. 4)
$z = 0$: non-slip wall

Solid

$x = 0$ and $x = X$: plane of symmetry
Other surfaces except fluid–solid interfaces: adiabatic

Fluid–solid interfaces

Non-slip, wall with heat transfer

where $P_i - P_o = \Delta P$. The pressure drop along the flow on one side of the heat exchanger is specified as the dimensionless pressure drop group defined as the Bejan number in Refs. [21,22]

$$\mathrm{Be}=\frac{\Delta P Z^2}{\mu\alpha} \tag{20}$$

The cases simulated numerically are listed in Table 1. To generate the temperature field and calculate the global heat transfer performance we used a finite-volume computational package [23] with pressure-based solver, cell-based gradient evaluation, SIMPLE algorithm for pressure–velocity coupling and second order upwind scheme for momentum and energy equations. In grid generation, hexahedron cells are adopted. We saved computational time by using two types of mesh sizes: a fine mesh for the fluid domains, and a nonuniform coarse mesh for the solid domains. Because the fluids are incompressible, the calculation of the flow field is decoupled from the temperature field. The solver performs iterations until the scaled residuals satisfy the following convergence criterion: the mass flow rates at all the inlets and outlets and temperatures at all the outlets are monitored until their relative changes in a specified time interval (namely, 200 iterations) are less than 10^{-5} and 10^{-4}, respectively. In addition, the mesh independence was checked before each simulation was performed. Less than 1% changes in mass flow rates and 1% changes in heat transfer rates between successive mesh sizes are considered acceptable results. Successive mesh sizes mean that the number of loops in-

Table 1
Cases selected for numerical simulation.

Case	d (mm)	Z (mm)	n	ϕ	h (mm)	Be	Sv	Solid material
1	10	2.8	2	0.06	1.2	6.51×10^2 to 6.51×10^5	5.4	Steel
2	10	2.8	3	0.06	1.2	1.42×10^3 to 1.42×10^6	7.3	Steel
3	10	2.8	4	0.06	1.2	3.32×10^3 to 3.32×10^6	9.5	Steel

Table 2
Cases selected for analysis.

Case	d (mm)	Z (mm)	n	ϕ	h (mm)	Sv
1	10	2.8	2	0.02–0.1	0.4–1.2	4.6–7.8
2	10	2.8	3	0.02–0.1	0.4–1.2	6.2–10.5
3	10	2.8	4	0.02–0.1	0.4–1.2	8–13.7

creases by about 1/3 from one mesh to the next. The number of cells used in the simulations varies from case to case. For example, the number of cells for tree-shaped structure of case 1 in Table 1, which meets the mesh independence requirement, is 1,209,822 (755,128 for fluid and 454,694 for solid).

The numerical simulation of the flow field permits the calculation of the global mass flow rate

$$\dot{m} = \dot{m}_a + \dot{m}_b \tag{21}$$

Because the counterflow is balanced, the global heat transfer rate q can be calculated by analyzing one of the streams, for example, the hot stream

$$q_h = q_{ha} + q_{hb} = \sum_{j=1}^{2^n} \dot{m}_{aij} c_p (T_{hin} - T_{haoj}) + \dot{m}_b c_p (T_{hi} - T_{hbo}) \tag{22}$$

We also calculated the heat transfer rate received by the cold stream, q_c, and in subsequent calculations of the performance we used the average $q = (q_h + q_c)/2$. For all the cases, the discrepancy between q_h and q_c was found to be less than 0.2%.

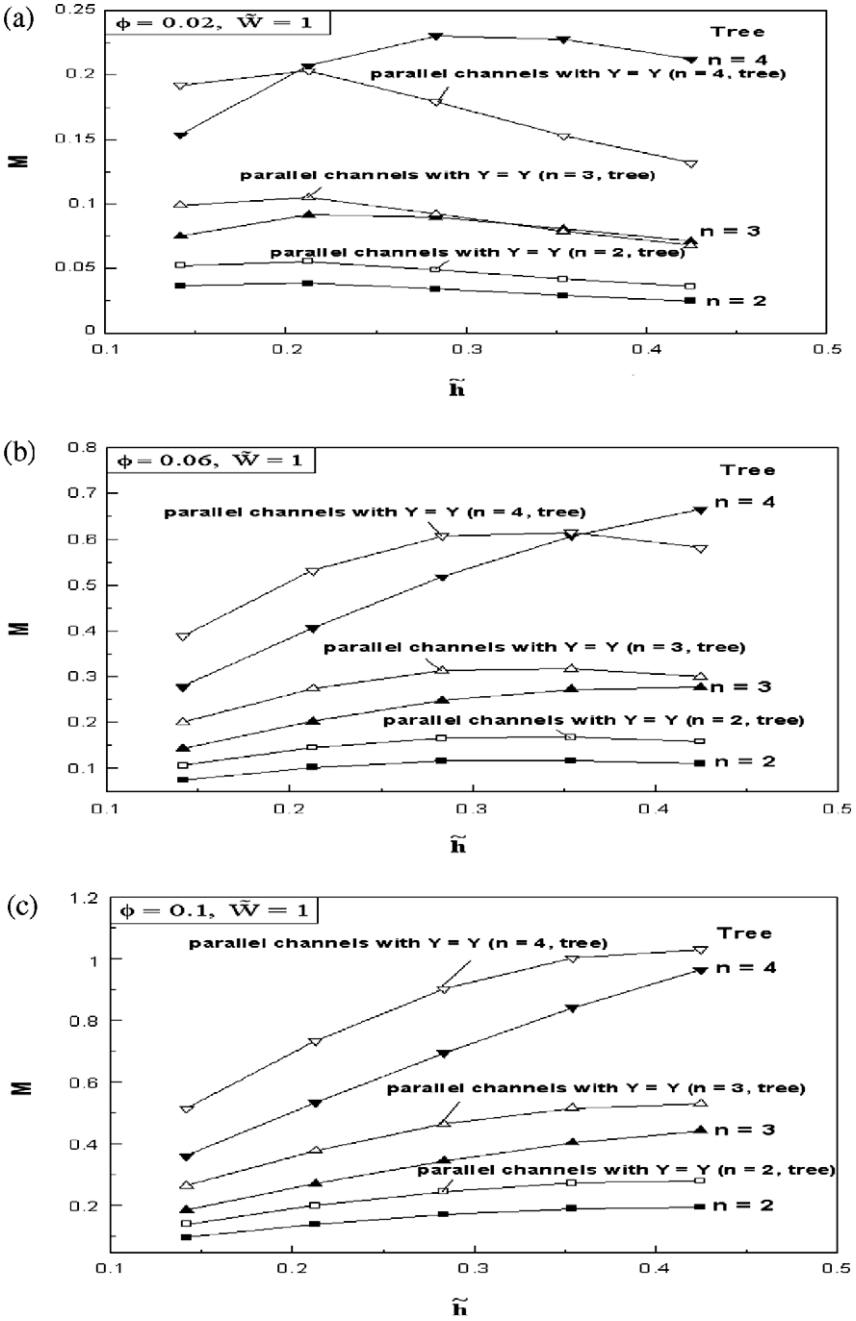

Fig. 5. Dimensionless flow rate based on analysis with fixed per-unit-volume pumping power ($\widetilde{W} = 1$).

Because the dimensions of tree-shaped vascularized bodies with various pairing levels (n) are numerous, a direct comparison of competing designs (flow rates, heat transfer rates) is difficult. To start, we must define the proper dimensionless parameters for comparing the performance of tree-shaped structures with different pairing numbers. Considering that Z and t (or h) are the same in all the cases (Table 1), we define the following dimensionless parameters

$$\widetilde{W} = \dot{W}''' \frac{Z^4}{(k\mathrm{Nu}/c_\mathrm{p})^2(\nu/\rho)} = \frac{\dot{W}}{XYZ}\frac{Z^4}{(k\mathrm{Nu}/c_\mathrm{p})^2(\nu/\rho)} \tag{23}$$

$$M = \frac{\dot{m}c_\mathrm{p}}{k\mathrm{Nu}Z} \tag{24}$$

$$\widetilde{R} = \frac{(T_{hi} - T_{ci})k_{\mathrm{steel}}Z}{q} \tag{25}$$

where $\widetilde{W}$ is based on the pumping power required per unit volume and M and $\widetilde{R}$ are based on the capacity rate and thermal resistance of the entire volume.

4. Analytical results

Based on the analytical calculation and the dimensionless expression of flow rate, Eq. (24), we can compare quantitatively the flow resistance characteristics of elemental units (Fig. 3) with various n. Table 2 shows the cases used in the analysis on flow rates. Figs. 5 and 6 show the effect of pairing number n, depth h and porosity ϕ on M when the per-unit-volume pumping power and the pressure drop are fixed, respectively. When $\widetilde{W}$ is fixed (Fig. 5), in the range of $\tilde{h} = 0.14$–0.43 (i.e. $h = 0.4$–1.2 mm) and $\phi = 0.02$–0.1, the flow rate M increases as the number of pairing

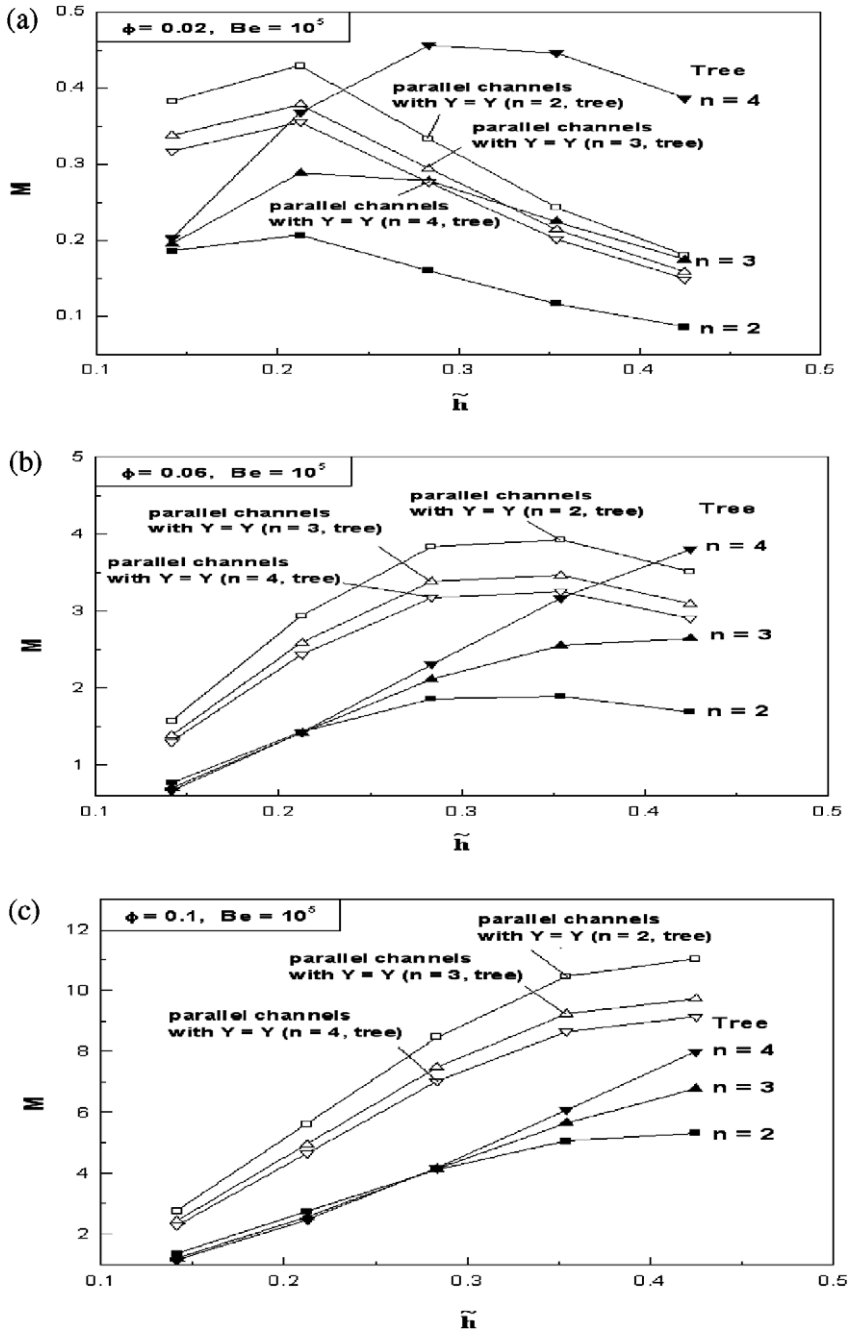

Fig. 6. Dimensionless flow rate based on analysis with fixed pressure drop ($\mathrm{Be} = 10^5$).

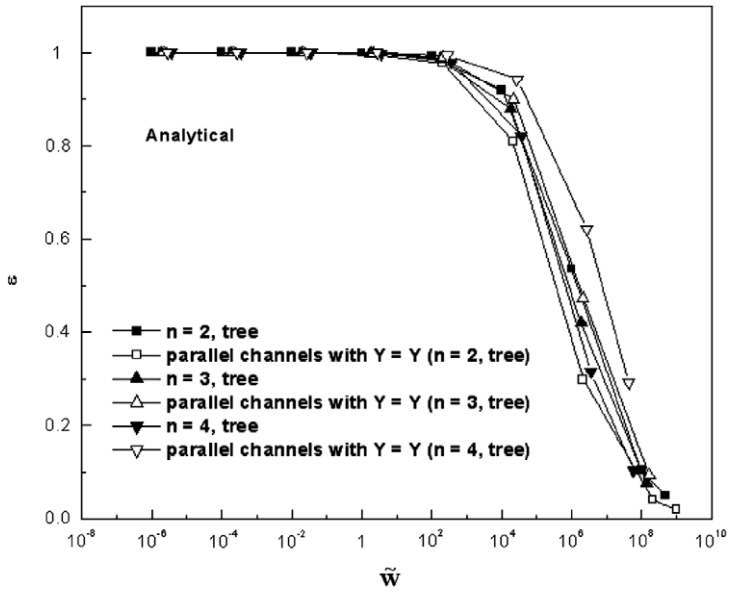

Fig. 7. Effectiveness determined based on analysis for the cases shown in Table 1, but with a wider Reynolds number range: 8.89×10^{-5}–1956 ($n = 2$, tree), 2.24×10^{-4}–1945 ($n = 3$, tree), 4.93×10^{-4}–1971 ($n = 4$, tree) and 8.73×10^{-4}–1952 (parallel channels).

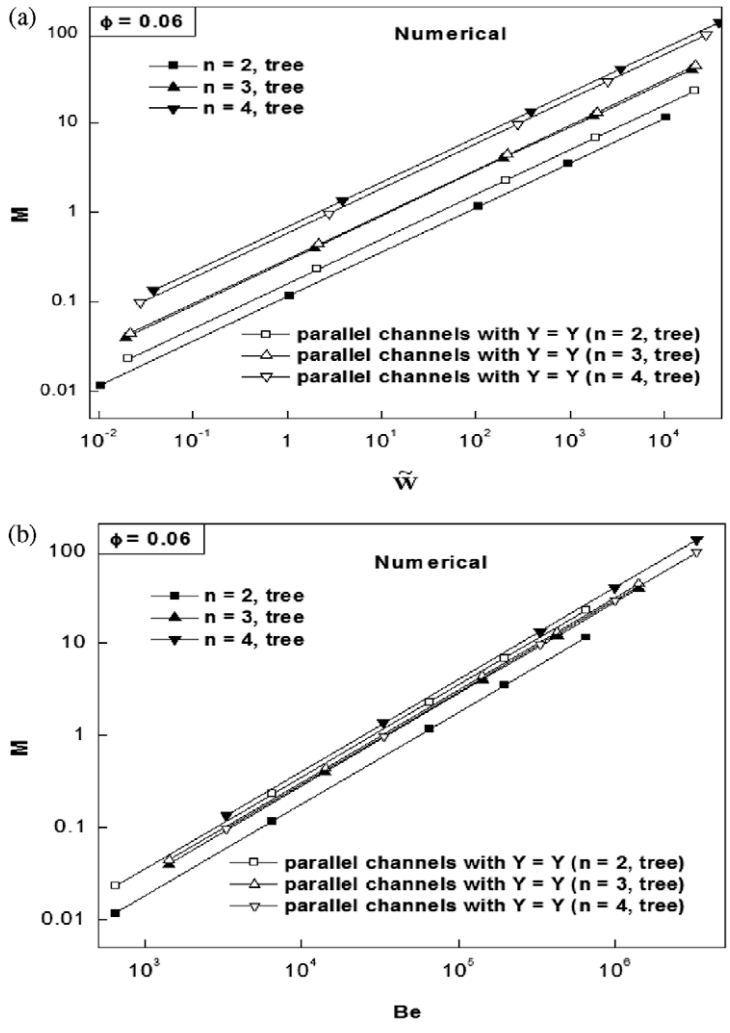

Fig. 8. Dimensionless flow rate based on numerical simulations for the cases shown in Table 1. Reynolds number range: 9.39×10^{-3}–9.32 ($n = 2$, tree), 0.024–23.5 ($n = 3$, tree), 0.053–51 ($n = 4$, tree), 9.46×10^{-3}–9.38 [parallel channels with $Y = Y$ ($n = 2$, trees)], 9.61×10^{-3}–9.57 [parallel channels with $Y = Y$ ($n = 3$, trees)] and 0.011–10.87 [parallel channels with $Y = Y$ ($n = 4$, trees)].

levels n increases. When Be is fixed (Fig. 6), the range in which M increases as the number of pairing levels n increases becomes smaller than that in Fig. 5. Another difference between Figs. 5 and 6 is that the corresponding reference channels display various features when the dimensions are different. When $\widetilde{W}$ is fixed (Fig. 5), the flow rate M increases as the size or volume of parallel channels increases. When Be is fixed (Fig. 6), the flow rate M decreases as the size or volume of parallel channels increases Figs. 5 and 6 confirm that if the depth is properly designed, trees become increasingly attractive in offering greater access to flow as their number of branching levels increases.

Fig. 7 shows the analytical results for effectiveness in the geometries in Table 1. The highest Reynolds numbers for all the structures do not exceed the 1900–2000 range, which ensures that the flow regime is laminar. The effectiveness drops as the dimensionless pumping power $\widetilde{W}$ exceeds the range 1–10^2. When $\widetilde{W}$ is less than 1, the effectiveness is practically equal to 1. This limit is valid for all the architectures shown in Fig. 7.

In the range $\widetilde{W} = 10^2$–10^7, when the element size increases (i.e. when n increases for trees) the effectiveness of trees decreases and the effectiveness of parallel channels increases (Fig. 7). For example, the effectiveness of parallel channels is greater than that of the trees with $n = 4$. This means that parallel channels approach their ideal heat transfer conditions more closely than trees ($q \to q_{max}$) when n increases. Because various tree-shaped structures and parallel channels have different q_{max} values, a larger ε does not represent a higher heat transfer rate or lower thermal resistance ($\widetilde{R}$).

In conclusion, the analysis shows that from the point of view of effectiveness parallel channels are preferable when complex trees have many levels of bifurcation. Trees are preferable when the levels of bifurcation are low. This conclusion was checked by the numerical simulations reported in the next section.

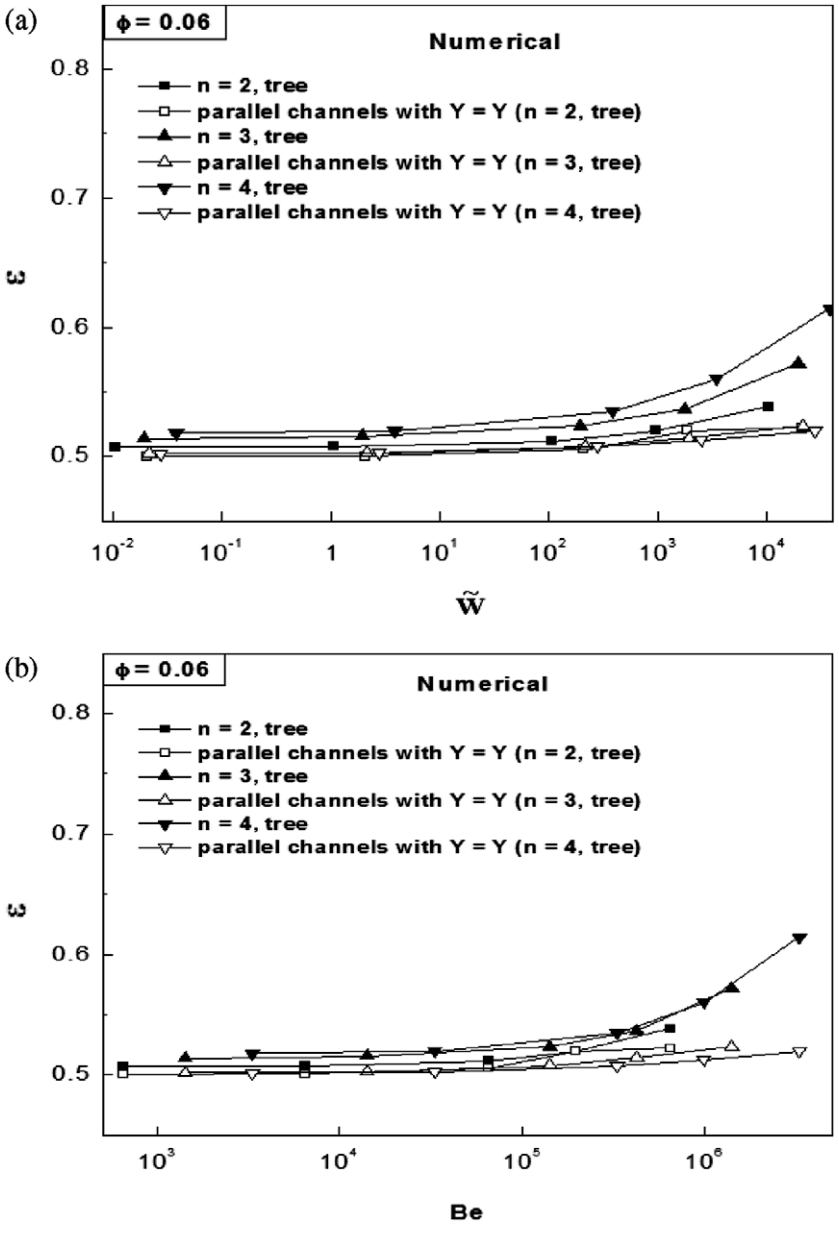

Fig. 9. Effectiveness based on numerical simulations for the cases shown in Table 1. Reynolds number range: 9.39×10^{-3}–9.32 ($n = 2$, tree), 0.024–23.5 ($n = 3$, tree), 0.053–51 ($n = 4$, tree), 9.46×10^{-3}–9.38 [parallel channels with $Y = Y$ ($n = 2$, trees)], 9.61×10^{-3}–9.57 [parallel channels with $Y = Y$ ($n = 3$, trees)] and 0.011–10.87 [parallel channels with $Y = Y$ ($n = 4$, trees)].

5. Numerical results

Fig. 8 shows the dimensionless flow rates obtained numerically for the geometries selected in Table 1. If the available pumping power $\widetilde{W}$ is specified (Fig. 8a), tree-shaped structures with larger n (or higher complexity) offer greater flow access. Only when n is larger than a critical value (namely, $n > 3$ in Fig. 8a), tree-shaped structures are better than parallel channels. For both trees and parallel channels, larger units (e.g., $n = 4$ tree design and its corresponding parallel-channels design) offer greater flow access than smaller units. These results agree well with the analytical results (cf. Fig. 5).

If the pressure drop is specified (Fig. 8b), the conclusion for tree-shaped structures still holds but the performance gap between different trees ($n = 2$, 3 and 4) narrows. For parallel channels, however, smaller units (e.g., parallel channels corresponding to $n = 2$ tree) offer greater flow access if Be is specified, which also agrees well with the analytical results (cf. Fig. 6).

Fig. 9 shows the ε—$\widetilde{W}$ and ε–Be results for tree-shaped structures and parallel channels with steel as the solid material. At low pumping power levels (e.g., $\widetilde{W} < 10^2$ in Fig. 9a), the effectiveness increases slightly as $\widetilde{W}$ increases. When $\widetilde{W}$ is large, the effectiveness increases significantly. This increase is slower for parallel channels. The effectiveness of larger tree units (with more pairing levels) is greater than that of smaller units (with fewer pairing levels) when the pumping power or pressure drop is specified. For example, the effectiveness increases by 6% when $\widetilde{W} = 1000$ and n increases from $n = 2$ to $n = 4$. In the range shown in Fig. 9, the effectiveness of tree-shaped designs is greater than the effectiveness of parallel channels with the same unit dimensions.

When the pumping power for parallel channels is specified (Fig. 9a), the effectiveness of larger units is approximately the same as that of smaller units in the given range. When the pressure drop is specified (Fig. 9b), the effectiveness of smaller units is slightly greater than that of larger units in the range $Be > 10^5$, although in the range $Be < 10^5$ they are nearly the same.

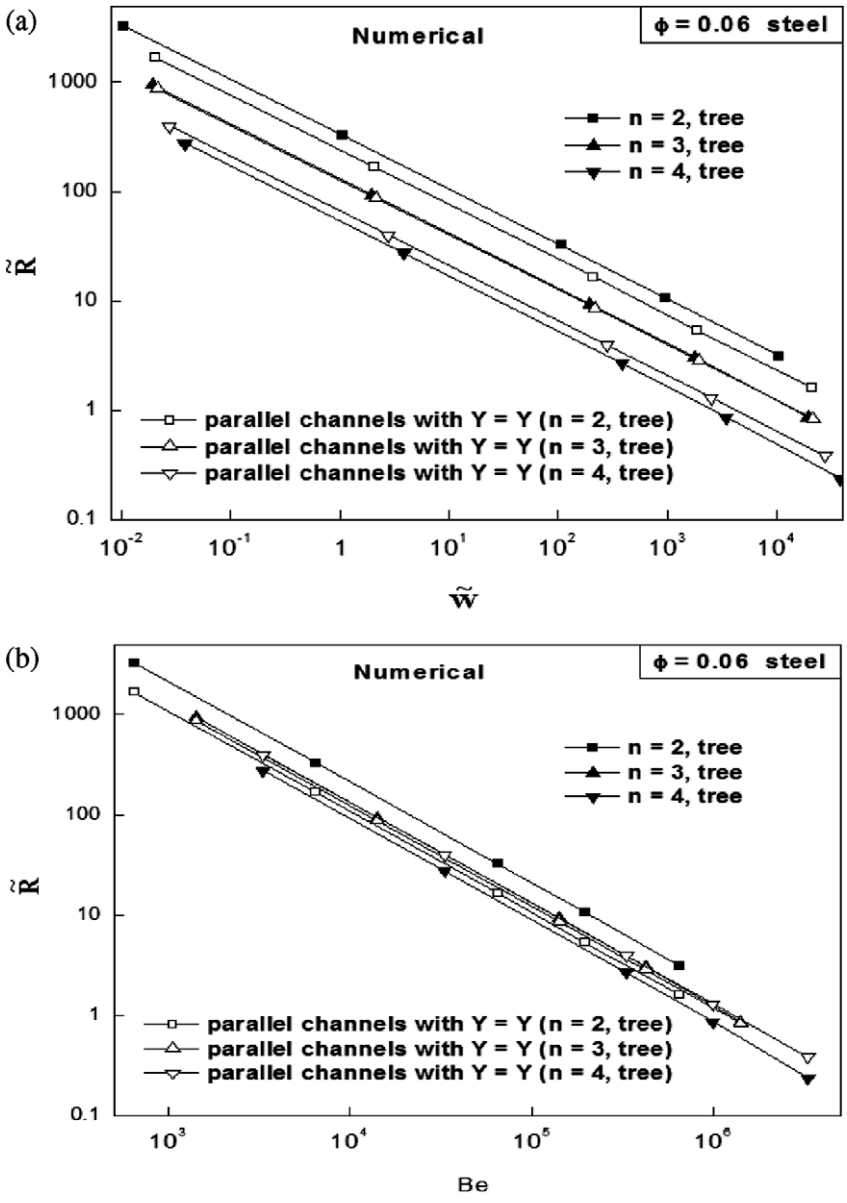

Fig. 10. Dimensionless thermal resistance based on numerical simulations for the cases shown in Table 1. Reynolds number range: 9.39×10^{-3}–9.32 ($n = 2$, tree), 0.024–23.5 ($n = 3$, tree), 0.053–51 ($n = 4$, tree), 9.46×10^{-3}–9.38 [parallel channels with $Y = Y$ ($n = 2$, trees)], 9.61×10^{-3}–9.57 [parallel channels with $Y = Y$ ($n = 3$, trees)] and 0.011–10.87 [parallel channels with $Y = Y$ ($n = 4$, trees)].

Figs. 7 and 9a show that the analytical and numerical results have different characteristics in the $\widetilde{W}$ range 10^{-2}–10^{4}. When $\widetilde{W}$ increases, the analytical ε decreases but the numerical ε increases. The discrepancy between the analytical and numerical values means that the analytical method used in conventional counterflow heat exchangers is not applicable. Instead, a three-dimensional heat transfer and fluid flow simulation (with conduction in the solid) is necessary for calculating the heat transfer performance of the tree-shaped heat exchangers proposed in this paper.

Fig. 10a shows the effect of $\widetilde{W}$ and n on the thermal resistance $\widetilde{R}$. For all the tree-shaped structures and parallel channels that we studied, $\widetilde{R}$ decreases while $\widetilde{W}$ increases. This trend is in accordance with the results of Ref. [15]. Another observation is that tree-shaped structures with higher n offer greater heat transfer ability (smaller $\widetilde{R}$). When n is higher than a critical value (e.g., $n = 4$ in Fig. 10a), tree-shaped structures perform better than parallel channels in the specified $\widetilde{W}$ range. When n is lower (e.g., $n = 2$ in Fig. 10a), tree-shaped structures perform worse than parallel channels. By combining Figs. 8a and 10a, we see that if the available pumping power is specified, structures offering greater access for fluid flow also provide greater access for heat flow. This point is important in practice, because it simplifies the search for better multi-objective flow architectures.

Fig. 10b shows the effect of Be and n on the thermal resistance $\widetilde{R}$. The conclusion is the same as for tree structures (Fig. 10a), although the performance gap between different tree designs is smaller. For parallel channels, however, $\widetilde{R}$ increases slightly while the dimensions of units increase when Be is specified.

6. The effect of conduction in the solid

We showed in Figs. 5 and 6 that tree-shaped structures are preferable when the porosity of the structure (ϕ) is small. We also showed that the neglect of the effect of heat conduction in the solid material can lead to unrealistic results. We studied the effect of solid conduction in greater detail. Fig. 11 shows the effect of the solid thermal conductivity k_s on ε and $\widetilde{R}$ (case 3, Table 1) when $n = 4$ and

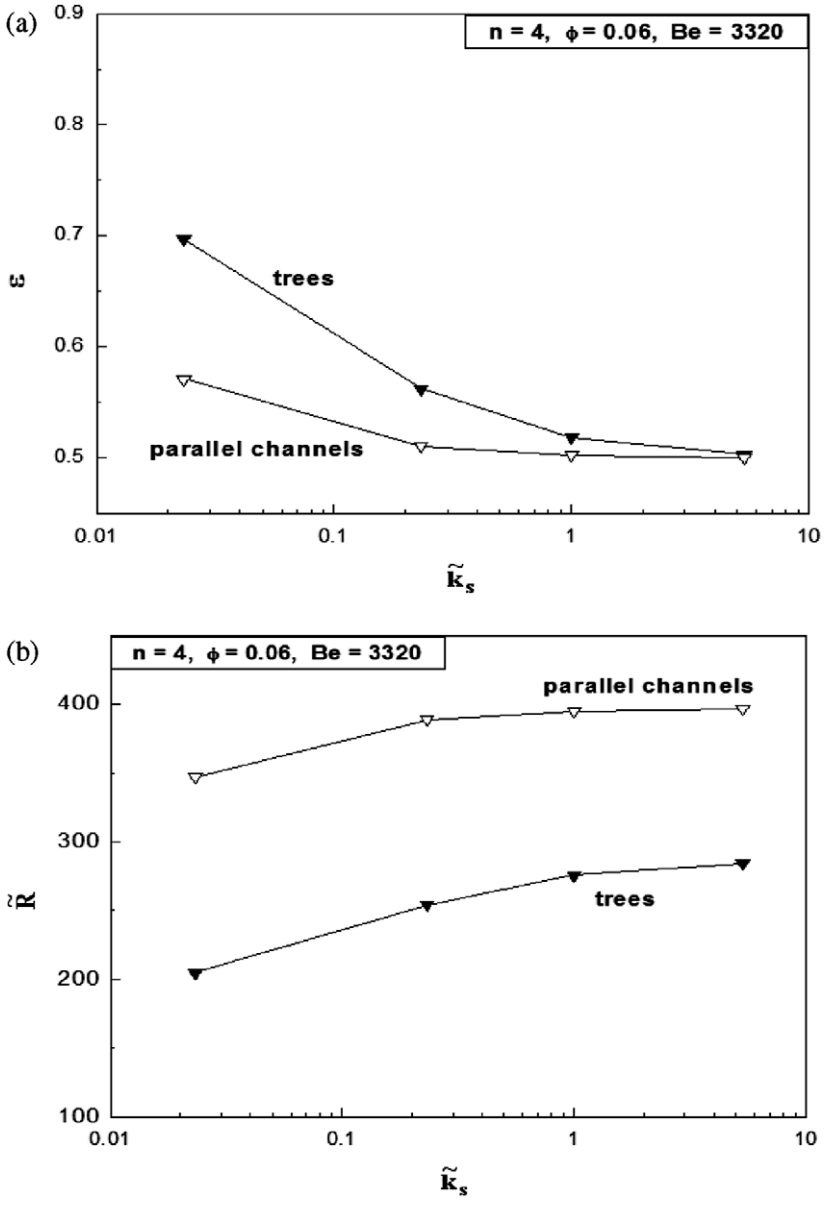

Fig. 11. The effect of solid thermal conductivity.

Be = 3320. The other properties of the solid material (density, specific heat) are assumed to be the same as for steel.

Fig. 11a shows that in the $\tilde{k}_s$ range 0.023–5.35 [which corresponds to k_s = 1–230 W/(mK)], ε decreases as $\tilde{k}_s$ increases. This is true for trees and parallel channels. The effectiveness of tree-shaped structures with $n = 4$ is larger than for parallel channels. The ε gap between trees and parallel channels narrows as $\tilde{k}_s$ increases. In Fig. 11b, because of the greater flow access, tree structures offer smaller thermal resistance than parallel channels in the entire $\tilde{k}_s$ range.

Because in the limit $\tilde{k}_s \to 0$ the effectiveness ε drops to zero and $\tilde{R}$ tends to infinity, we expect a maximum ε (or a minimum $\tilde{R}$) in the range $0 < \tilde{k}_s < 0.023$. For the cases shown in Fig. 11, the wall thickness (t) is very small, and this means that the effect of wall thermal resistance (t/k_s) becomes significant only for very poor heat conducting materials. The results shown in Fig. 11 indicate that there are two important ways to enhance heat transfer in tree-shaped heat exchangers with small fluid porosity: (1) designing a better flow structure (i.e. with greater M and smaller flow resistance) to enhance the heat transfer between two streams, and (2) decreasing the longitudinal heat conduction in the solid material.

7. Heat transfer nonuniformity

Because the bifurcations of tree-shaped fluid channels are not symmetrical, the splitting of mass flow and heat convection is nonuniform. We define the fluid temperature nonuniformity at the tree outlets ($i = n$) as

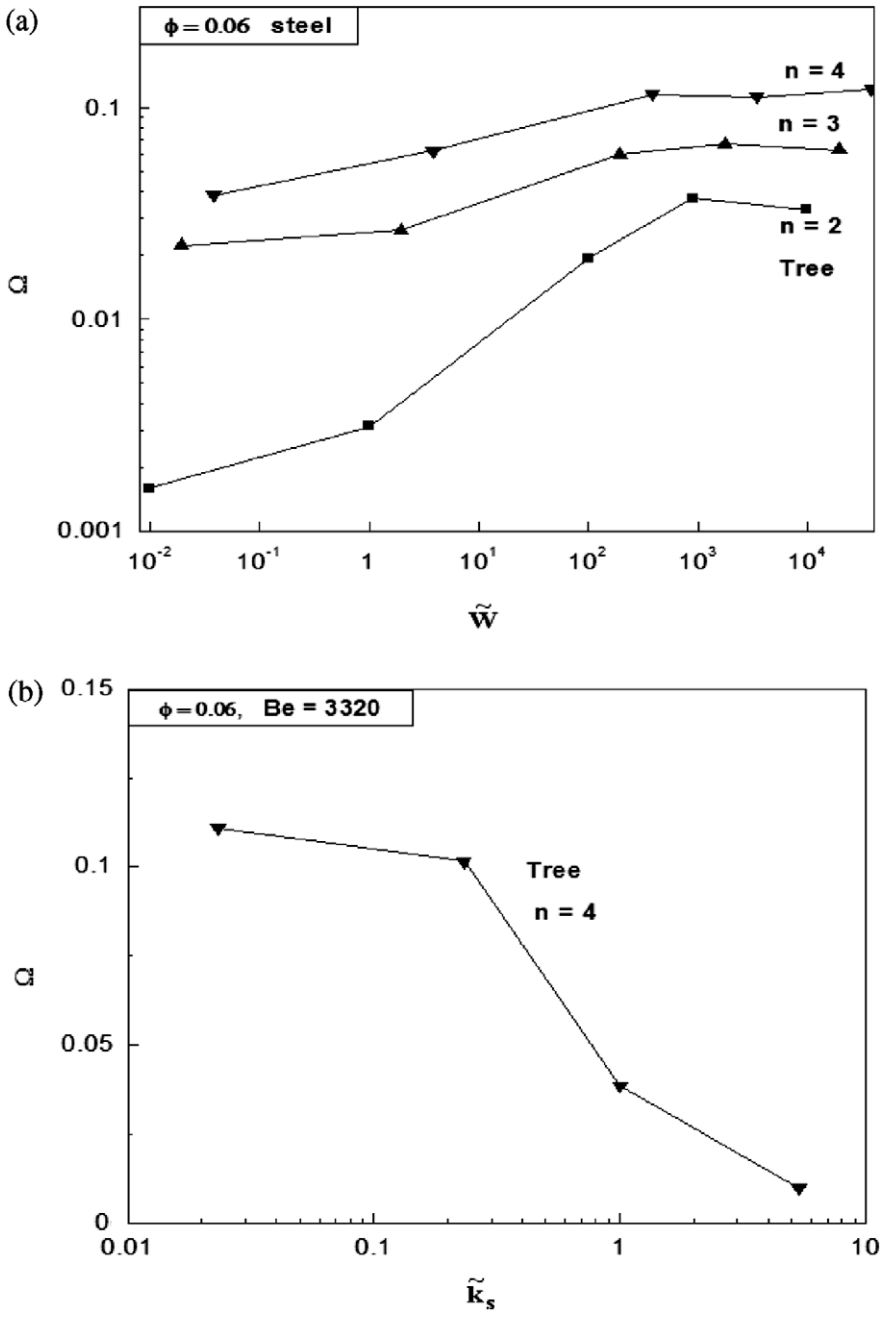

Fig. 12. Outlet fluid temperature nonuniformity (trees a and b, hot fluid, $n = 4$, Be = 3320, steel, Table 1).

$$\Omega = \frac{T_{\mathrm{fo,max}} - T_{\mathrm{fo,min}}}{|T_{\mathrm{fo,ave}} - T_{\mathrm{fi}}|} \tag{26a}$$

$$\Omega_{\mathrm{a}} = \left(\frac{T_{\mathrm{fo,max}} - T_{\mathrm{fo,min}}}{|T_{\mathrm{fo,ave}} - T_{\mathrm{fi}}|}\right)_{\mathrm{a}} \tag{26b}$$

In Eq. (26a), $T_{\mathrm{fo,max}}$ and $T_{\mathrm{fo,min}}$ represent the highest and lowest outlet fluid temperatures at the 2^n extremities of tree a and the single (thick) outlet of tree b (see Fig. 2, middle). In Eq. (26b), $T_{\mathrm{fo,max}}$ and $T_{\mathrm{fo,min}}$ represent the highest and lowest outlet fluid temperatures at the 2^n extremities of tree a. Because the tree-shaped heat exchanger is balanced, only the hot side of the heat exchanger is used for the illustration.

Fig. 12 shows the outlet fluid temperature nonuniformity Ω determined based on numerical simulations. We see that Ω increases with $\widetilde{W}$ (Fig. 12a) except at $\widetilde{W} = 9.9 \times 10^3$ (or Be = 6.5 × 10^5, Re = 9.32) for the $n = 2$ tree and $\widetilde{W} = 1.9 \times 10^4$ (or Be = 1.4×10^6, Re = 9.57) for the $n = 3$ tree. This change in pattern is due to the fact that the flow distribution in the fluid channels of the same rank changes while Be increases. For example, Be = 6.5×10^5 (Re = 9.32) for the $n = 2$ tree is the range beyond which the flow distribution and the position of the maximum $\dot{m}_{aj}$ change from $j = 2$ to $j = 3$. Furthermore, larger n values correspond to larger nonuniformity. Fig. 12b shows that in the $\tilde{k}_s$ range 0.023–5.35, the nonuniformity decreases with the increasing $\tilde{k}_s$ because high heat conduction in the x direction in the solid enhances the heat exchange between the fluid channels of the same rank. By combining Figs. 11b and 12b, we see that the nonuniformity decreases as $\tilde{k}_s$ increases, and the thermal resistance increases because it enhances the longitudinal heat conduction in solid, which decreases the heat transfer rate (or $|T_{\mathrm{fo,ave}} - T_{\mathrm{fin}}|$ in

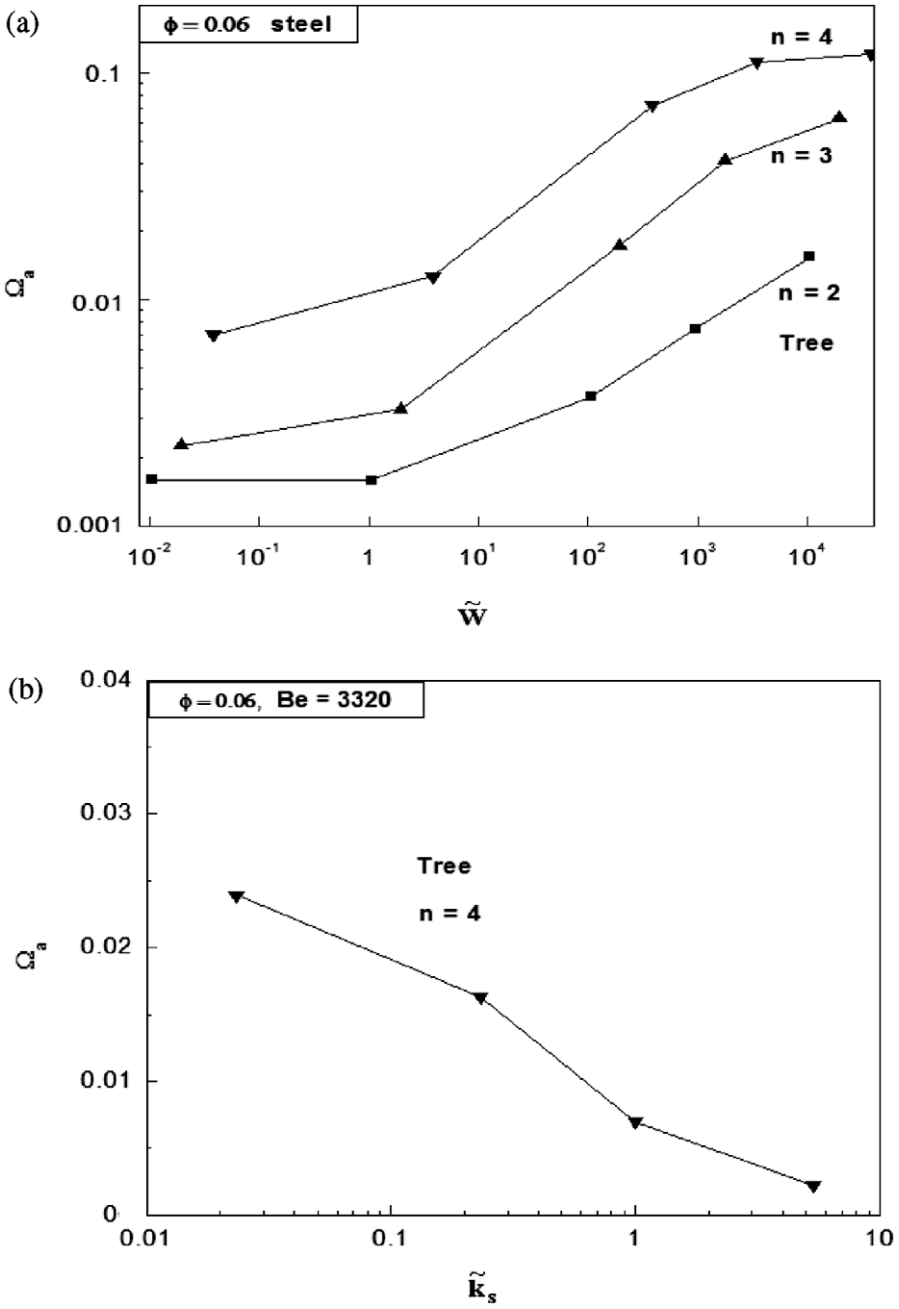

Fig. 13. Outlet fluid temperature nonuniformity (tree a, hot fluid, $n = 4$, Be = 3320, Table 1).

Eq. (26a)). The results show that the solid heat conduction in all directions (x, y, z) affects the performance of tree-shaped structures.

Fig. 13 shows the outlet fluid temperature nonuniformity Ω_a of tree a. For $n = 2$ and 3, and when $\widetilde{W} < 100$, the nonuniformity Ω_a is negligible (Fig. 13a). When $\widetilde{W} > 100$, Ω_a increases significantly with $\widetilde{W}$. In the entire range shown in Fig. 13a, the Ω_a of the trees with larger n is greater than that of the trees with smaller n. The effect of $\tilde{k}_s$ on Ω_a (Fig. 13b) is similar to the effect on Ω. Note that Ω_a is smaller than Ω for the cases shown in Figs. 12b and 13b.

In sum, the heat transfer nonuniformity Ω (or Ω_a) is determined by several factors: the pairing number n or the fluid channel structures, the power consumption $\widetilde{W}$ (or Be) and the solid thermal conductivity $\tilde{k}_s$. In practice, the balance between $\widetilde{R}$ and Ω (or Ω_a) is necessary.

One example of the temperature field is shown in Fig. 14. The results are for the upper surface (hot stream side) of the entire unit. In the regions far from the fluid channels, the temperature gradient is smaller than that close to the fluid channels. Because of the effect of longitudinal heat conduction in the solid, the longitudinal temperature gradient in the solid is smaller than in the fluid.

Fig. 15 shows the distribution of temperatures over the 17 outlets of the line-to-line tree structure with $n = 4$. Each temperature

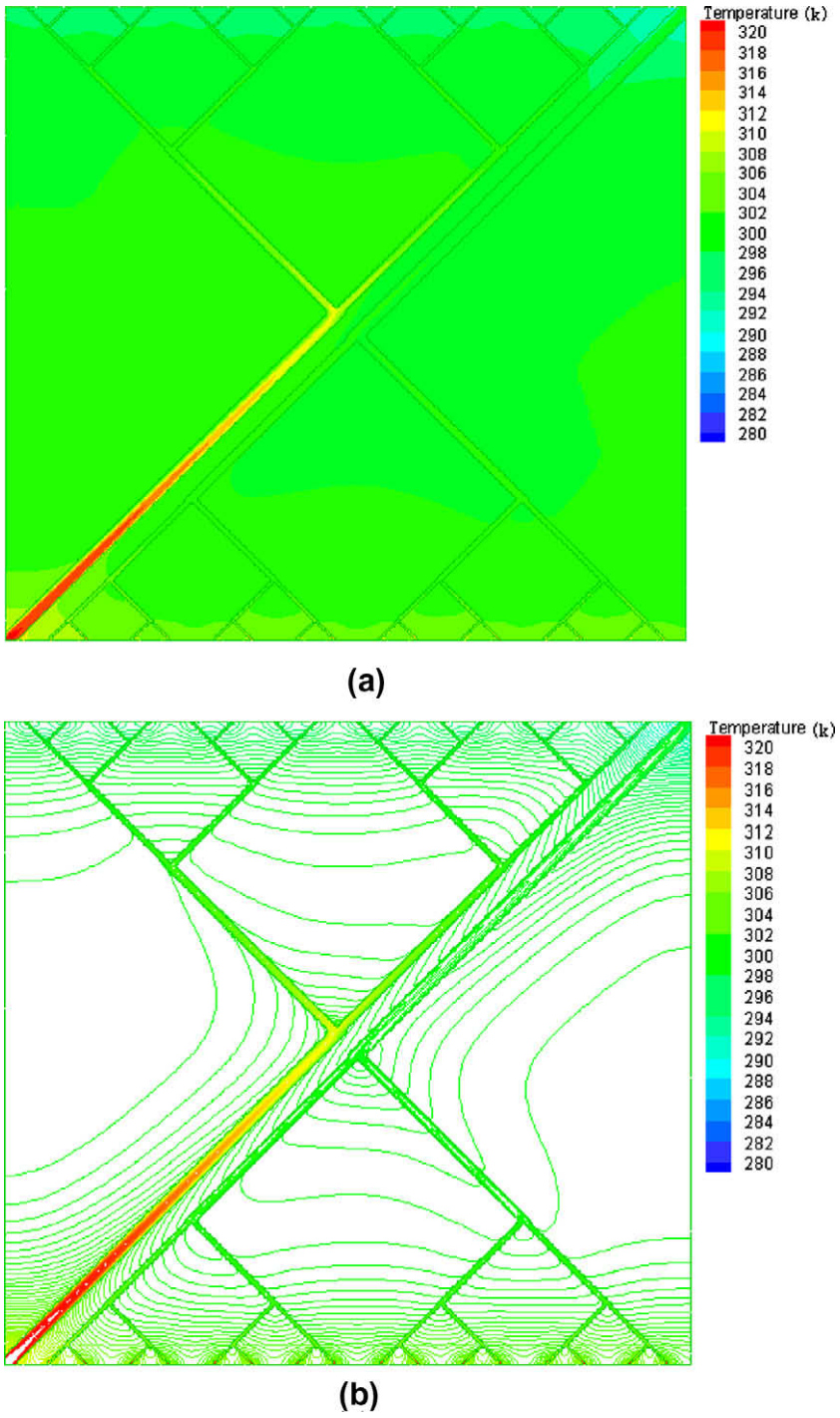

Fig. 14. Temperature distribution ($T_{hot,in} = 320$ K, $T_{cold,in} = 280$ K, $n = 4$, Be $= 3.32 \times 10^6$, steel, Table 1). (a) Temperature field image of the upper surface of the unit. (b) Isothermal curves on the upper surface of the unit.

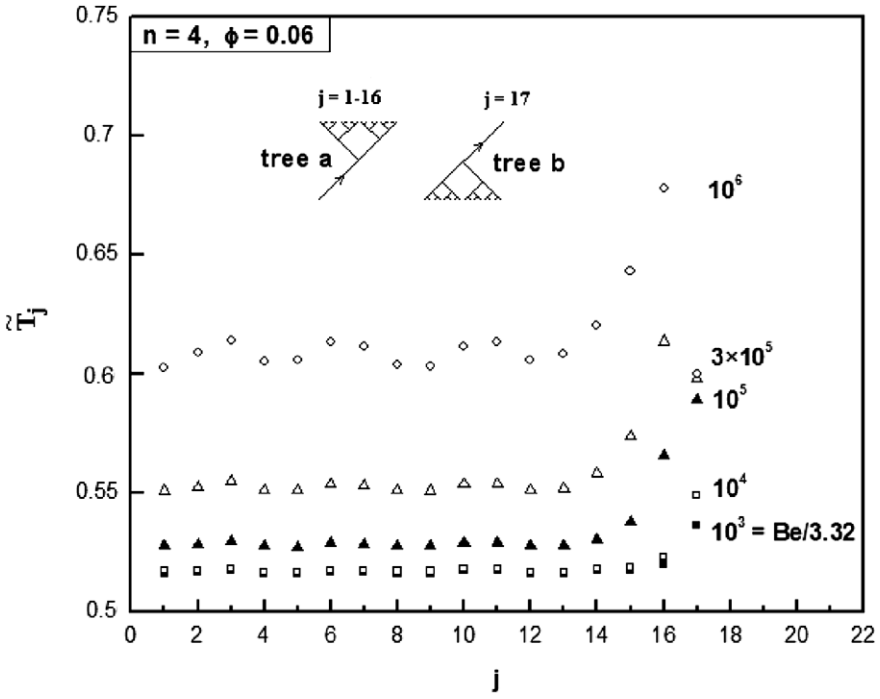

Fig. 15. Outlet temperatures of hot fluid ($T_{hot,in}$ = 320 K, $T_{cold,in}$ = 280 K, n = 4, Be = 3.32 × 10^6, steel, Table 1).

is the mean (bulk) temperature in the outlet cross-section. For the canopies close to the trunk of tree b (e.g., j = 13–17 for Be = 3.32 × 10^6), the nonuniformity of $\tilde{T}_j = (T_{hot,in} - T_{hot,out,j})/(T_{hot,in} - T_{cold,in})$ is more significant than that far from the trunk of tree b (e.g., j = 1–13 for Be = 3.32 × 10^6). This feature is due to the strong mass flow nonuniformity and geometrical asymmetry in the region close to the trunk of tree b.

8. Conclusions

In this paper we used three-dimensional numerical simulations to document the heat transfer performance of vascular designs with tree architectures. The map of thermal resistance versus pumping power was constructed. The results showed that there are two design domains. If the available pumping power is specified, tree vascularizations with more pairing levels (n) offer greater heat flow access than trees with less pairing levels. When the number of pairing levels is increased above a critical value (n > 3), tree vascularization offers greater heat flow access than parallel channels. Better flow structures provide greater heat transfer ability.

If the available pressure drop is specified, the conclusion for trees is the same as when the available pressure drop is specified. The difference is that the performance gap between different trees is smaller.

The effect of longitudinal heat conduction in the solid is significant. When $\tilde{k}_s$ increases in the range 0.023–5.35, the heat transfer effectiveness (ε) decreases and the thermal resistance ($\tilde{R}$) increases. This holds for both tree vascularizations and parallel channels.

The nonuniformity of outlet fluid temperatures is an important feature of tree-shaped vascular designs. Parallel channels do not have this feature, unless other effects such as blockage and temperature dependent properties cause flow maldistribution. The results also show that the temperature nonuniformity is negligible when the number of pairing levels is low (e.g., n = 2 or 3) and the available pumping power is small (Re < 1). When the number of pairing levels is high (e.g., n = 4) and the available pumping power is large, the nonuniformity is significant and cannot be neglected.

The numerical results show that the neglect of heat conduction in the solid leads to different analytical ε results than in the numerical simulations. In practice then, three-dimensional numerical simulations are recommended, especially for cases where the fluid porosity is small or the fraction of solid is large.

Acknowledgements

This research was supported by the Air Force Office of Scientific Research with a grant for "Constructal Technology for Thermal Management of Aircraft", and a MURI grant for the development of "Micro-Vascular Autonomic Composites" (University of Illinois at Urbana Champaign, Duke University, and University of California, Los Angeles). We thank Dr. David Moorhouse (Air Force Research Laboratory) for the advice and guidance that he gives us in this research direction. Dr. Houlei Zhang's visit at Duke University was supported by a grant from the China Scholarship Council and his work is also supported by Chinese National Foundation of Science (No. 50776046).

References

[1] A. Bejan, S. Lorente, Design with Constructal Theory, Wiley, Hoboken, 2008.
[2] A. Bejan, S. Lorente, K.-M. Wang, Network of channels for self-healing composite materials, J. Appl. Phys. 100 (2006) 033528.
[3] S.-W. Kim, S. Lorente, A. Bejan, Vascularized materials: tree-shaped flow architectures matched canopy to canopy, J. Appl. Phys. 100 (2006) 063525.
[4] K.-M. Wang, S. Lorente, A. Bejan, Vascularized networks with two optimized channels sizes, J. Phys. D: Appl. Phys. 39 (2006) 3086–3096.
[5] A. Bejan, Constructal-theory network of conducting paths for cooling a heat generating volume, Int. J. Heat Mass Transfer 40 (1997) 799–816.
[6] A. Bejan, M.R. Errera, Deterministic tree networks for fluid flow: geometry for minimal flow resistance between a volume and one point, Fractals 5 (1997) 685–695.
[7] Y. Chen, P. Cheng, Heat transfer and pressure drop in fractal tree-like microchannel nets, Int. J. Heat Mass Transfer 45 (2002) 2643–2648.
[8] Y. Chen, P. Cheng, An experimental investigation on the thermal efficiency of fractal tree-like microchannel nets, Int. Commun. Heat Mass Transfer 32 (2005) 931–938.
[9] Y. Chen, P. Cheng, Development on fractal tree-like microchannel heat sink, J. Eng. Thermophys. 27 (2006) 853–855 (in Chinese).
[10] A. Bejan, Advanced Engineering Thermodynamics, third ed., Wiley, Hoboken, 2006 (Chapter 13).

[11] A. Bejan, Shape and Structure, from Engineering to Nature, Cambridge University Press, Cambridge, UK, 2000. pp. 60–62.
[12] A.H. Reis, Constructal theory: from engineering to physics, and how flow systems develop shape and structure, Appl. Mech. Rev. 59 (2006) 269–282.
[13] A. Bejan, Dendritic constructal heat exchanger with small-scale crossflows and larger-scale counterflows, Int. J. Heat Mass Transfer 45 (2002) 4607–4620.
[14] V.A.P. Raja, T. Basak, S.K. Das, Heat transfer and fluid flow in a constructal heat exchanger, in: R.K. Shah, M. Ishizuka, T.M. Rudy, V.V. Wadeka (Eds.), Proceedings of the Fifth International Conference on Enhanced, Compact and Ultra-compact Heat Exchangers: Science, Engineering and Technology, Hoboken, NJ, USA, 2005, pp. 147–153.
[15] A.K. da Silva, S. Lorente, A. Bejan, Constructal multi-scale tree-shaped heat exchangers, J. Appl. Phys. 96 (2004) 1709–1718.
[16] A.K. da Silva, A. Bejan, Dendritic counterflow heat exchangers experiments, Int. J. Therm. Sci. 45 (2006) 860–869.
[17] S. Lorente, A. Bejan, Heterogeneous porous media as multiscale structures for maximum flow access, J. Appl. Phys. 100 (2006) 114909.
[18] H. Zhang, S. Lorente, A. Bejan, Vascularization with trees that alternate with upside-down trees, J. Appl. Phys. 101 (2007) 094904.
[19] S. Lorente, A. Bejan, Svelteness, freedom to morph, and constructal multi-scale flow structures, Int. J. Therm. Sci. 44 (2005) 1123–1130.
[20] R.K. Shah, A.L. London, Laminar flow forced convection in ducts, Adv. Heat Transfer 14 (Suppl. 1) (1978) 203–205.
[21] S. Bhattacharjee, W.L. Grosshandler, The formation of a wall jet near a high temperature wall under microgravity environment, ASME HTD-96 (1988) 711–716.
[22] S. Petrescu, Comments on "The optimal spacing of parallel plates cooled by forced convection", Int. J. Heat Mass Transfer 37 (1994) 1283.
[23] FLUENT, version 6.2, User's Manual, Fluent, Inc.